MPC-based DC-link voltage control for enhanced high-voltage ride-through of offshore DFIG wind turbine

Wei, Juan; Li, Canbing; Wu, Qiuwei; Zhou, Bin; Xu, Da; Huang, Sheng

Published in:
International Journal of Electrical Power & Energy Systems

Link to article, DOI:
10.1016/j.ijepes.2020.106591

Publication date:
2020

Document Version
Peer reviewed version

MPC-based DC-link voltage control for enhanced high-voltage ride-through of offshore DFIG wind turbine

Juan Wei[a,b], Canbing Li[a,b,*], Qiuwei Wu[c,*], Bin Zhou [a,b,*], Da Xu[a,b], Sheng Huang[c]

[a]*College of Electrical and Information Engineering, Hunan University, Changsha 410082, China*
[b]*Hunan Key Laboratory of Intelligent Information Analysis and Integrated Optimization for Energy Internet, Hunan University, Changsha 410082, China*
[c]*Centre for Electric Power and Energy, Department of Electrical Engineering, Technical University of Denmark, Lyngby 2800, Denmark*

Abstract

To deal with the DC-link overvoltage during high-voltage ride-through (HVRT) of the wind turbine, a coordinated DC-link voltage control (CDVC) scheme is proposed for enhancing the HVRT performance of offshore doubly-fed induction generator (DFIG) wind turbines equipped with the supercapacitor energy storage system (SESS). This scheme is formulated as a two-stage control problem depending on the depth of grid voltage swell, which can prevent damaging the converter resulting from the insufficient reactive support in the first stage, and achieve efficient coordinated control under various magnitude and timescale of grid voltage swell. In the first stage, considering the dynamic behavior of the DFIG during HVRT, a voltage-dependent reactive current control (VRCC) scheme is designed to regulate the current reference of the wind turbine. The first stage aims to supply fast reactive current support without the DC chopper. In the second stage, once the DC-link voltage exceeds the predefined threshold, a coordinated control scheme considering the SESS and the wind turbine operation is implemented using model predictive control (MPC), aiming to regulate the excessive active power by tracking the current reference from the first stage. The proposed control scheme is validated in PSCAD/EMTDC under various operational scenarios. Case study results show that the proposed scheme can effectively mitigate the DC-link overvoltage and enhance HVRT capability under asymmetrical and symmetrical voltage swells.

Highlights

A two-stage coordinated control scheme is proposed for enhancing the HVRT capability of offshore wind turbines.
A voltage-dependent reactive current control is designed to achieve fast reactive current support.
An MPC-based SESS control scheme is developed to regulate the active power output.

Keywords

DC-link voltage control, high-voltage ride-through (HVRT), supercapacitor energy storage system (SESS), doubly fed induction generator (DFIG), offshore wind power, renewable energy.

*Corresponding author at: Center for Electric Power and Energy, Department of Electrical Engineering, Technical University of Denmark, Kongens Lyngby2800, Denmark.
E-mail addresses: qw@elektro.dtu.dk (Q. Wu); licanbing@sjtu.edu.cn (C. Li); binzhou@hnu.edu.cn (B. Zhou).

1. Introduction

Offshore wind power has been developing dramatically in recent years due to better wind conditions and the challenge of global carbon emissions. According to the statistics from the Global Wind Energy Council (GWEC), the installed capacity of global offshore wind power has increased from approximately 4.12 GW in 2011 to 23.14 GW in 2018 and offshore wind energy has huge potential in Germany, China, and the UK [1], [2]. Moreover, the offshore wind farm capacity is growing, and the installed capacity is estimated to increase by more than four times, reaching 100 GW by 2025. The inherent intermittency and volatility of offshore wind energy have brought challenges to the secure operation of power systems, e.g., the voltage stability of power systems [3]-[6]. Extensive efforts have been made to enhance the low voltage ride through (LVRT) capability with different control schemes [7]-[13]. However, the impact of grid voltage swell on offshore wind turbines and relevant high voltage ride through (HVRT) strategies have not been fully investigated.

In an offshore wind farm, voltage swells can be initiated by energizing submarine cable, switching off large loads, charging capacitor banks, or unbalanced faults [14]-[16]. Reference [17] demonstrates a new phenomenon that the grid voltage swell may occur after successfully riding through low-voltage disturbances. If the wind turbine experiences a gird voltage swell event, the DC-link voltage will rapidly increase, which may further cause a series of transient problems such as rotor inrush current and torque oscillations [18]. However, it is hard to ride through deep voltage swell only relying on the wind turbine itself due to the current and voltage limits of the converters.

The conventional solution is to add external auxiliary equipment to improve the HVRT capability, and protection or control countermeasures are taken to successfully ride through disturbances and avoid large-scale cascading trip of offshore wind turbines. A vector-based hysteresis current regulator was used to mitigate the rotor current oscillations and improve the fault-ride-through performance of DFIG-based wind turbines [19]. In [20], a chopper protection circuit was used to consume excessive power and maintain stable DC-link voltage, which reduces the wind power system efficiency due to the heat losses of the resistor. In [21], a virtual impedance control strategy was proposed to mitigate the rotor current oscillation and improve the HVRT capability of the wind power system. For the wind farm, the grid voltage is compensated to restore the normal level by using static synchronous compensator (STATCOM) or other compensation systems [22], [23]. In [24], the coordination of series dynamic resistor devices and crowbar protection was adopted to reduce rotor circuit overvoltage and limit the overcurrent in large-scale offshore wind farms. Nevertheless, previous control schemes have mainly been verified for their feasibility and effectiveness in stator or rotor current control and stability issues, and little work has been done on the DC-link voltage control for DFIG wind turbines during the HVRT.

The alternative solution for the HVRT is to connect an additional energy storage system (ESS) [25] at the DC-link of the power electronic converters for balancing the extra power and preventing overvoltage at the DC bus. Various storage technologies, such as the flywheel, supercapacitor (SC), batteries and superconducting magnetic energy storage (SMES), have been integrated with renewable energy generation (REG) for power fluctuation reduction [26], [27], and the flexibility provided can be utilized to mitigate the effect of variable renewable energy source (RES). In [28], the coordinated control between the DFIG-based wind turbine and distributed ESS was developed to regulate the active power for the fatigue load reduction. The supercapacitor energy storage system (SESS), as a new type of energy storage in recent years, has been widely applied to REG due to higher power density, much longer life cycle, and faster dynamic response. The SESS was used in [29] to increase the penetration of REG integrated into weak grids, and it was shown that the SESS is more suitable for wind energy integration than other storage systems due to the much higher life cycle and fast dynamic response. Further studies on sizing and operation management of the SESS for firming wind power were conducted in [30]. However, the above researches on the SESS for wind power integration are mainly based on the steady-state operation, aiming to smooth the fluctuating wind power and increase the penetration of renewable energy sources. The performance of the SESS under grid voltage swells and the interactions between the SESS and wind turbines during HVRT have not been studied yet.

In this paper, a coordinated DC-link voltage control scheme is proposed for HVRT capability enhancement of offshore DFIG wind turbines. The contributions of this paper are summarized as follows: 1) Considering the grid voltage swell magnitude, a two-stage CDVC control scheme is proposed to control the wind turbine and SESS for mitigating DC-link overvoltage; 2) A voltage-dependent reactive current control is implemented to provide fast reactive current support by regulating the reactive current reference of the offshore DFIG wind turbines without the DC chopper; 3) An MPC-based SESS control scheme is formulated to regulate the active power output for mitigating the DC-link fluctuation, thereby enhancing HVRT capability of offshore DFIG wind turbines.

The paper is organized as follows. The problem formulation and modeling of offshore DFIG wind turbines during voltage swell are described in Section 2. A voltage-dependent reactive current control for the wind turbine is presented in Section 3. A CDVD scheme during the HVRT of the wind turbine is detailed in Section 4. Comparative studies for the HVRT of DFIG wind turbines between the proposed coordinated control scheme and other traditional control schemes are provided in Section 5, followed by the conclusions.

2. Modeling and Analysis of Offshore Wind Turbines During HVRT

In order to study the dynamics of DC-link voltage in DFIG wind turbines during the grid voltage swell, it is necessary to establish a model to represent the system. The schematic diagram of the SESS-integrated DFIG-based offshore wind farm is shown in Fig. 1. All wind turbines are connected to the POC through the 33/220kV main transformer, and to the onshore grid by the AC transmission cables. Here, the DC-link model is a capacitor connected in parallel between the rotor-side converter (RSC) and GSC to maintain the normal operation of the back-to-back converters. The primary function of the SESS is to absorb/release the unbalanced power and facilitate the DC-link to smooth the DC-link voltage, while the phase-locked loop (PLL) is widely employed to synchronize DFIG wind turbines with the grid. The active and reactive power flow direction of offshore DFIG wind turbines and the current direction are shown in Fig. 1. For simplicity, power electronics losses and line losses are neglected.

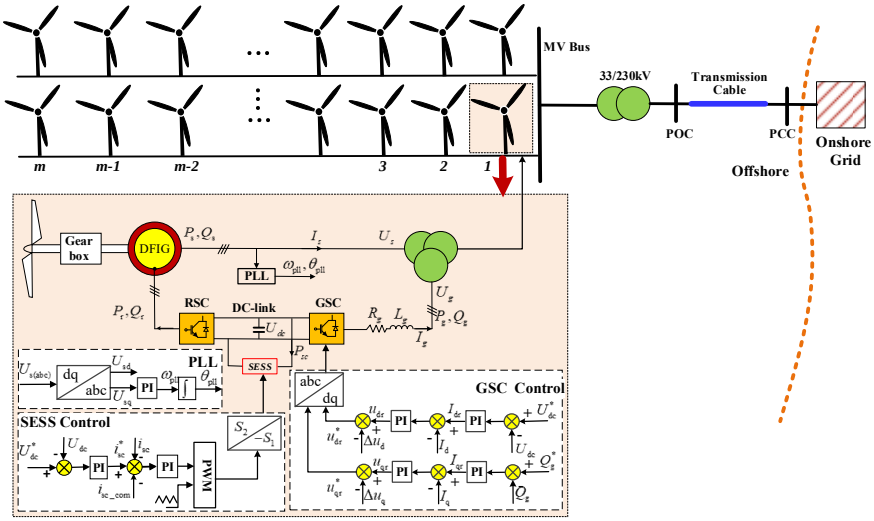

Fig.1 Topology diagram of SESS-integrated DFIG-based offshore wind farm.

2.1 Problem Formulation during HVRT

When an asymmetric voltage swell occurs, the DC-link voltage of the wind turbine will increase with the grid voltage increasing. The DC-link overvoltage results in high mechanical and electrical stress for the back-to-back converters, which may endanger the secure operation of the wind turbine. Thus, the wind turbine should initiate a controlled voltage drop for mitigating DC-link overvoltage. Fig.2 shows the response curves of the offshore wind turbine during the HVRT. In Fig. 2(a), after the grid voltage U_{g} exceeds its threshold $U_{\mathrm{g}}^{\mathrm{thres}}$ at t_1, the voltage-dependent reactive current control (VRCC) is activated by the GSC

to supply fast reactive current support. Note that $U_{\mathrm{g}}^{\mathrm{thres}} = 1.1U_{\mathrm{N}}$. In Fig.2(b), the DC-link voltage U_{dc} begins to increase at t_1. Once U_{dc} exceeds its threshold value $U_{\mathrm{dc}}^{\mathrm{thres}}$ at t_2, the coordinated control scheme based on the MPC is activated by the SESS to reduce the excessive power. At t_3, U_{dc} rises to the maximum value while the SESS output power is balanced with the excessive power. When the grid swell event is cleared at t_4, U_{dc} gradually recovers to the feasible range.

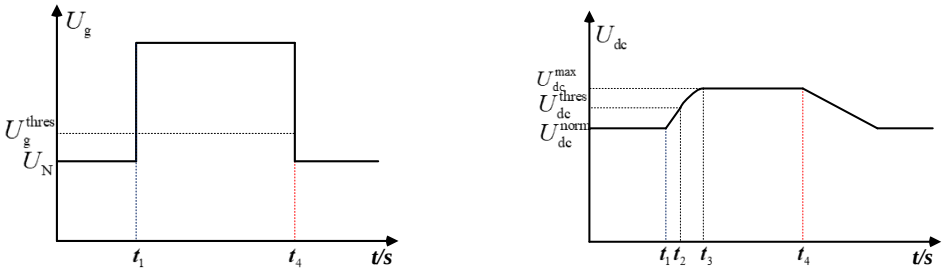

(a) Grid voltage at PCC (b) DC-link voltage

Fig 2. Schematic response curves of the offshore wind turbine for a grid voltage swell.

After the grid voltage swells, the GSC of offshore DFIG wind turbine is mainly controlled to inject/release reactive current into the power grid according to the grid code requirement. From Fig. 1, the power and voltage of the DFIG-based wind turbine can be described as,

$$\begin{bmatrix} P_{\mathrm{g}} \\ Q_{\mathrm{g}} \end{bmatrix} = \frac{3}{2}\begin{bmatrix} u_{\mathrm{gd}} & u_{\mathrm{gq}} \\ u_{\mathrm{gq}} & -u_{\mathrm{gd}} \end{bmatrix}\begin{bmatrix} i_{\mathrm{gd}} \\ i_{\mathrm{gq}} \end{bmatrix} \tag{1}$$

$$U_{\mathrm{g}} = V_{\mathrm{g}} + \mathrm{j}\omega_{\mathrm{g}} L_{\mathrm{g}} I_{\mathrm{g}} + I_{\mathrm{g}} R_{\mathrm{g}} \tag{2}$$

where P_{g} and Q_{g} are the active and reactive power delivered to the grid; U_{g} and I_{g} are the voltage and current of the grid side; the subscripts d and q are the corresponding d-axis and q-axis components in the positive synchronously rotating frame, respectively; V_{g} is the space vectors of the GSC output terminal voltage; R_{g} and L_{g} are the three-phase GSC resistance and inductance, respectively; and ω_{g} is the synchronous angular frequency.

Based on (2), the GSC voltage is expressed in the positive synchronously rotating frame as,

$$\begin{cases} u_{\mathrm{gd}} = R_{\mathrm{g}} i_{\mathrm{gd}} - \omega_{\mathrm{g}} L_{\mathrm{g}} i_{\mathrm{gq}} + v_{\mathrm{gd}} \\ u_{\mathrm{gq}} = R_{\mathrm{g}} i_{\mathrm{gq}} + \omega_{\mathrm{g}} L_{\mathrm{g}} i_{\mathrm{gd}} + v_{\mathrm{gq}} \end{cases} \tag{3}$$

Considering the limited GSC capacity, the relationship between the GSC voltage and DC-link voltage can be described as,

$$V_{\mathrm{g}} = \sqrt{v_{\mathrm{gd}}^2 + v_{\mathrm{gq}}^2} \le \frac{U_{\mathrm{dc}}}{m} \tag{4}$$

where m is the modulation ratio. In this paper, the SPWM mode is adopted and (4) can be rewritten as,

$$\frac{2}{U_{\mathrm{dc}}}\sqrt{v_{\mathrm{gd}}^2 + v_{\mathrm{gq}}^2} \le 1 \tag{5}$$

In (3), the GSC operates in the stator voltage-oriented control mode under the normal operation, and the q-axis voltage can be simplified to be zero. Based on (4), (5) and neglecting R_{g}, the DC-link voltage is constrained as,

$$U_{\mathrm{dc}} \ge 2\sqrt{\left(U_{\mathrm{g}} + \omega_{\mathrm{g}} L_{\mathrm{g}} i_{\mathrm{gq}}\right)^2 + \left(-\omega_{\mathrm{g}} L_{\mathrm{g}} i_{\mathrm{gd}}\right)^2} \tag{6}$$

2.2 Modeling and Capacitance Calculation of SESS

Under voltage swell, the wind turbine operates in the HVRT operation. Conventionally, the wind turbine is required to stay

connected to the power grid and inject reactive current to support grid voltage recovery. The HVRT requirement for wind turbines in Australia is shown in Fig. 3(a) [31]. The reactive current injection requirement of the German E. ON NetZ code, shown in Fig. 3(b) [32], is adopted.

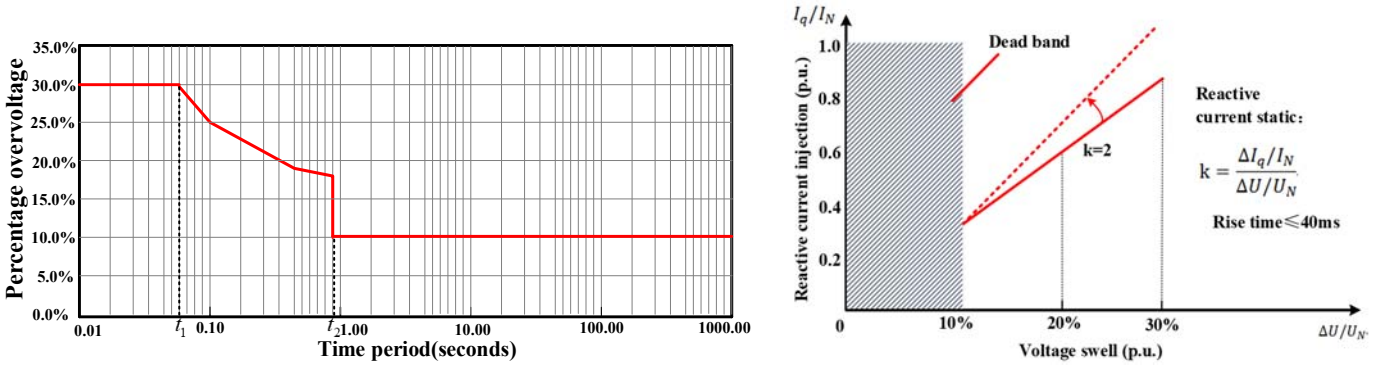

(a) HVRT capability for the tolerance of voltage swells (b) Requirement of reactive current support

Fig. 3. Grid code requirement.

According to the grid code requirements, as given in Fig. 3, the reactive current support can be calculated as the area below the HVRT curve and above 1.1 $p.u.$ line. The absorbed/supplied power of the SESS is comprehensively evaluated based on the voltage swell magnitude and the reactive current requirement.

Fig. 4 shows the dynamic model of the SESS, which consists of the bidirectional DC-DC converter, filter inductance and the equivalent model of the SC. Here, the bidirectional DC-DC converter handles the charging/discharging of the SC, whereas the filter inductance is to suppress the influence of short-time inrush-current during charging. Depending on the grid transient characteristic as well as fast charging/ discharging, the SC is equivalent to an ideal capacitor C_{SC} in series with an equivalent resistor R_{SC}, and R_{SC} reflects the energy loss of the SC.

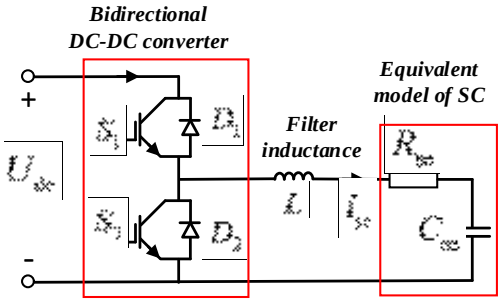

Fig 4. The schematic diagram of the SESS.

Compared to onshore wind farms, the wind speed of offshore wind farms is relatively uniform due to stable wind distribution and lower terrain effects [33], and thus the effect of wind speed changes on power output is not considered. Assume that the power captured by offshore DFIG wind turbines is the rated power P_{e} and remains unchanged during the HVRT, the total wind energy from the RSC $E_{\mathrm{RSC\_in}}$ can be expressed as,

$$E_{\mathrm{RSC\_in}} = P_{\mathrm{e}} t_{\mathrm{HVRT}} \tag{7}$$

where t_{HVRT} is the total time of the HVRT. The SC capacity is chosen considering the energy stored in the driving train of the DFIG. The maximum energy $E_{\mathrm{DR\_max}}$ stored in the DFIG driving train is calculated as,

$$E_{\mathrm{DR\_max}} = \frac{1}{2} J(\omega_{\mathrm{max}}^2 - \omega_{\mathrm{e}}^2) \tag{8}$$

where J is the moment of inertia; and $\omega_{\max}$ and ω_{e} are the maximum and rated angular speed of the DFIG.

Based on (7) and (8), the minimum energy $E_{\mathrm{Dl\_min}}$ injected from the RSC can be formulated as,

$$E_{\mathrm{Dl\_min}} = E_{\mathrm{RSC\_in}} - E_{\mathrm{DR\_max}} = P_{e}t_{\mathrm{HVRT}} - \frac{1}{2}J(\omega_{\max}^{2} - \omega_{e}^{2}) \tag{9}$$

Then, the power injected from the RSC is expressed as,

$$P_{\mathrm{Dl\_HVRT}} = -P_{r} = \frac{E_{\mathrm{Dl\_min}}}{t_{\mathrm{HVRT}}} = \frac{1}{t_{\mathrm{HVRT}}}\left[P_{e}t_{\mathrm{HVRT}} - \frac{1}{2}J(\omega_{\max}^{2} - \omega_{e}^{2})\right] \tag{10}$$

Meanwhile, based on active power in (1) and the reactive current requirement in compliance with the HVRT curve, the active power injected from the GSC during HVRT period can be calculated as,

$$P_{g} = \begin{cases} \sqrt{3}U_{g}\sqrt{I_{\max}^{2} - 4\left(\dfrac{U_{g}}{U_{N}} - 1\right)^{2} I_{N}^{2}}, & U_{g} \in (1.1U_{N}, 1.18U_{N}) \\ \sqrt{3}U_{e}\sqrt{I_{\max}^{2} - 4\left(\dfrac{-0.12}{t_{2}-t_{1}}t + \dfrac{1.3t_{2}-1.18t_{1}}{t_{2}-t_{1}} - 1\right)^{2} I_{\max}^{2}} \times \left(\dfrac{-0.12}{t_{2}-t_{1}}t + \dfrac{1.3t_{2}-1.18t_{1}}{t_{2}-t_{1}}\right), & U_{g} \in [1.18U_{N}, 1.3U_{N}) \\ 1.3\sqrt{3}U_{e}\sqrt{I_{\max}^{2} - 0.36I_{\max}^{2}}, & U_{g} = 1.3U_{N} \end{cases} \tag{11}$$

where U_{e} is the rms voltage of the grid line-to-line voltage. $I_{\max}$ is maximum permissible current of the GSC, which is usually set as 1.5 times of the rated current; and t is the duration of gird voltage swell.

To ensure the transient power balance of the DFIG wind turbines, the instantaneous active power required by the SESS is formulated as,

$$P_{\mathrm{SESS}} = P_{\mathrm{Dl\_HVRT}} - P_{g} \tag{12}$$

Then the storage energy of the SESS can be expressed as,

$$\begin{aligned} E_{\mathrm{sc}} &= \int_{0}^{t_{2}} P_{\mathrm{SESS}}\,dt \\ &= \int_{0}^{t_{1}} (P_{\mathrm{Dl\_HVRT}} - 1.3\sqrt{3}U_{e} \times \sqrt{I_{\max}^{2} - 0.36I_{\max}^{2}})\,dt \\ &+ \int_{t_{1}}^{t_{2}} (P_{\mathrm{Dl\_HVRT}} - \sqrt{3}U_{e} \times \sqrt{I_{\max}^{2} - 4\left((\dfrac{-0.12}{t_{2}-t_{1}}t + \dfrac{1.3t_{2}-1.18t_{1}}{t_{2}-t_{1}}) - 1\right)^{2} I_{\max}^{2}} \times (\dfrac{-0.12}{t_{2}-t_{1}}t + \dfrac{1.3t_{2}-1.18t_{1}}{t_{2}-t_{1}}))\,dt \end{aligned} \tag{13}$$

The stored energy of the SESS can be written as when ignoring the energy loss of the R_{SC},

$$E_{\mathrm{sc}} = \frac{1}{2}C_{\mathrm{sc}}U_{\mathrm{dc}}^{2} \tag{14}$$

Substituting (13) into (14), the required capacitance for the SESS can be determined by,

$$\begin{aligned} C_{\mathrm{sc}} = \frac{2}{U_{\mathrm{dc}}^{2}}\Bigg[& \int_{0}^{t_{1}} (P_{\mathrm{Dl\_HVRT}} - 1.3\sqrt{3}U_{e} \times \sqrt{I_{\max}^{2} - 0.36I_{\max}^{2}})\,dt \\ & + \int_{t_{1}}^{t_{2}} \left[P_{\mathrm{Dl\_HVRT}} - \sqrt{3}u_{e} \times \sqrt{I_{\max}^{2} - 4\left((\dfrac{-0.12}{t_{2}-t_{1}}t + \dfrac{1.3t_{2}-1.18t_{1}}{t_{2}-t_{1}}) - 1\right)^{2} I_{\max}^{2}}) \times (\dfrac{-0.12}{t_{2}-t_{1}}t + \dfrac{1.3t_{2}-1.18t_{1}}{t_{2}-t_{1}}) \right] dt \Bigg] \end{aligned} \tag{15}$$

3. Voltage-Dependent Reactive Current Control

Fig. 2(b) shows the requirement of the reactive current support according to the voltage condition. The reactive current in-

jected by the GSC according to the grid codes is calculated as,

$$i_{\mathrm{gq\_m}}=\begin{cases}0 & U_{\mathrm{g}}\in(0.9U_{\mathrm{N}},1.1U_{\mathrm{N}})\\ k\times\left(\dfrac{U_{\mathrm{g}}}{U_{\mathrm{N}}}-1\right)\times I_{\mathrm{N}}, & U_{\mathrm{g}}\in[1.1U_{\mathrm{N}},1.3U_{\mathrm{N}}]\end{cases} \tag{16}$$

where $i_{\mathrm{gq\_m}}$ is the reactive current injected from the GSC; U_{N} is the rated grid voltage; I_{N} is the rated current of the GSC; and k is an adjustable coefficient of reactive current, which should be no less than 2.

Based on (16) and considering that the phase angle θ_{g} is also the angle between reactive current and active current [34], the active current injected by the GSC is expressed as,

$$i_{\mathrm{gd\_m}}=\frac{i_{\mathrm{gq\_m}}}{\tan\theta_{\mathrm{g}}} \tag{17}$$

When the grid voltage swell occurs, the DFIG wind turbines are required to provide inductive reactive power within a specified period to bring the grid voltage back to the normal operation state. By adopting the stator voltage orientation in the positive synchronously rotating frame, the DC-link voltage is related to the GSC current, so it is important to regulate the reference value of i_{g}.

Based on (6), the reactive current of the GSC is calculated as,

$$i_{\mathrm{gq}}\le\frac{1}{\omega_{\mathrm{g}}L_{\mathrm{g}}}\left(\sqrt{\frac{U_{\mathrm{dc}}^2}{4}-\left(-\omega_{\mathrm{g}}L_{\mathrm{g}}i_{\mathrm{gd}}\right)^2}-U_{\mathrm{g}}\right) \tag{18}$$

Since the reactive current is mainly controlled by the reactive power, the effect of the active power can be ignored. Thus, the maximum reactive current i_{gqmax} can be formulated as,

$$i_{\mathrm{gqmax}}=\frac{0.5U_{\mathrm{dc}}-U_{\mathrm{g}}}{\omega_{\mathrm{g}}L_{\mathrm{g}}} \tag{19}$$

Under voltage swell, the unbalanced voltage may reduce the power/current delivery capability of the GSC. The peak GSC current amplitude is much higher than that of normal grid voltage, which might damage the GSC and affect the secure operation of the wind turbine. Thus, the maximum current limitation control of the GSC should be considered, and the amplitude of grid voltage is constrained as,

$$I_{\mathrm{g}}=\sqrt{i_{\mathrm{gd}}^2+i_{\mathrm{gq}}^2}\le I_{\max} \tag{20}$$

Fig. 5 shows the proposed voltage-dependent reactive current control scheme, which is integrated into the PI control loop to regulate the reactive current. Fig. 5(a) shows the time-domain response of the DC-link voltage. In Fig. 5(a), the DC-link voltage continues to increase along with the grid voltage swell. When U_{dc} exceeds the normal value $U_{\mathrm{dc}}^{\mathrm{norm}}$, the VRCC is activated by the GSC to reduce the active power. Fig. 5(b) illustrates the VRCC control curve. The relation between U_{dc} and i_{gq} can be designed as,

$$U_{\mathrm{dc}}-U_{\mathrm{dc}}^{\mathrm{thres}}=K_{\mathrm{HVRT}}(i_{\mathrm{gq}}-i_{\mathrm{gq\_m}}) \tag{21}$$

where $U_{\mathrm{dc}}^{\mathrm{thres}}$ is the threshold value of DC-link voltage; U_{N} is the grid nominal voltage; and K_{HVRT} is the droop coefficient.

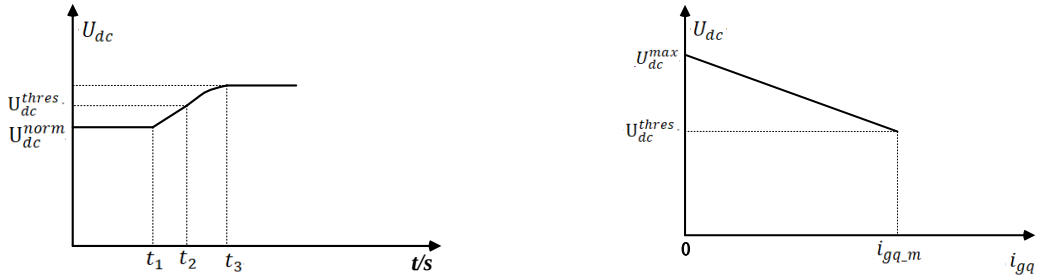

(a) DC-link voltage (b) VRCC control curve

Fig. 5. The VRCC scheme during HVRT.

4. Coordinated DC-link Voltage Control Strategy

4.1 Model Predictive Control of SESS

The SESS aims to mitigate the DC-link voltage fluctuation caused by the excessive active power during the HVRT. Since the power supplied or absorbed by the SESS is controlled by switching the buck-boost converter, it is necessary to obtain the effect of its switching on the power supplied/absorbed. Switches S1 and S2 are driven by a set of complementary signals. When SC discharges to supply power, the SESS operates in the boost mode. On the contrary, the SESS operates in the buck mode. Taking the boost mode as an example, as shown in Fig. 6, the predictive model can be formulated as,

$$\begin{cases} S_2=1, S_1=0: L_{\mathrm{sc}}\dfrac{dI_{\mathrm{sc}}}{dt}+R_{\mathrm{sc}}I_{\mathrm{sc}}=U_{\mathrm{sc}} \\ S_2=0, S_1=1: L_{\mathrm{sc}}\dfrac{dI_{\mathrm{sc}}}{dt}+R_{\mathrm{sc}}I_{\mathrm{sc}}=U_{\mathrm{sc}}-U_{\mathrm{dc}} \end{cases} \tag{22}$$

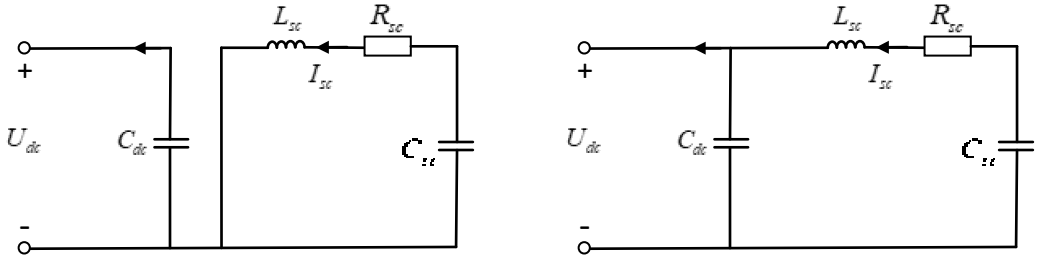

(a) $S_2=1, S_1=0$ (b) $S_2=0, S_1=1$

Fig. 6. Topologies of boost mode for the SESS.

The discrete-time model with a sampling time T_{sc} can be formulated as,

$$\begin{cases} S_2=1, S_1=0: I_{\mathrm{sc}}(k+1)=\dfrac{T_{\mathrm{sc}}}{L_{\mathrm{sc}}}\left[U_{\mathrm{sc}}(k)-R_{\mathrm{sc}}I_{\mathrm{sc}}(k)\right]+I_{\mathrm{sc}}(k) \\ S_2=0, S_1=1: I_{\mathrm{sc}}(k+1)=\dfrac{T_{\mathrm{sc}}}{L_{\mathrm{sc}}}\left[-U_{\mathrm{dc}}(k)+U_{\mathrm{sc}}(k)-R_{\mathrm{sc}}I_{\mathrm{sc}}(k)\right]+I_{\mathrm{sc}}(k) \end{cases} \tag{23}$$

Considering the relatively slow change of the SC voltage, the SC output power can be predicted as,

$$P_{\mathrm{sc}}(k+1)=\left|I_{\mathrm{sc}}(k+1)\times U_{\mathrm{sc}}(k)\right| \tag{24}$$

The required power supplied by the SESS to keep the power balance can be calculated as,

$$P_{\mathrm{SESS}}^{*}=\left|I_{\mathrm{SESS}}\times U_{\mathrm{dc}}^{\mathrm{ref}}\right| \tag{25}$$

where P_{SESS} and I_{SESS} denote the active power and current supplied or absorbed by the SESS; and $U_{\mathrm{dc}}^{\mathrm{ref}}$ denotes the DC-link voltage reference.

Assume that the deviation between U_{dc} and $U_{\mathrm{dc}}^{\mathrm{ref}}$ is linearized during HVRT, a prediction horizon N is introduced as the rolling decision steps. The voltage relationship between the next time slot $k+1$ and the N steps is described as,

$$U_{\mathrm{dc}}^{\mathrm{ref}}=U_{\mathrm{dc}}(k)+N\left[U_{\mathrm{dc}}(k+1)-U_{\mathrm{dc}}(k)\right] \tag{26}$$

The capacitor current in the next time slot $k+1$ can be written as,

$$I_{\mathrm{dc}}(k+1)=C_{\mathrm{dc}}\frac{U_{\mathrm{dc}}(k+1)-U_{\mathrm{dc}}(k)}{T_{\mathrm{sc}}}=\frac{C_{\mathrm{dc}}}{NT_{\mathrm{sc}}}(U_{\mathrm{dc}}^{\mathrm{ref}}-U_{\mathrm{dc}}(k)) \tag{27}$$

By applying the Kir-choff's current law, the relationship of the current between the DFIG and SESS can be formulated as,

$$I_{\mathrm{SESS}}=I_{\mathrm{r}}-I_{\mathrm{dc}}-I_{\mathrm{g}} \tag{28}$$

By combining (27) and (28), the SESS current can be predicted as,

$$I_{\mathrm{SESS}}(k+1)=I_{\mathrm{r}}(k)-I_{\mathrm{dc}}(k+1)-I_{\mathrm{g}}(k) \tag{29}$$

The following cost function should be minimized,

$$J_{\mathrm{P}}=\left|P_{\mathrm{SESS}}^{*}(k+1)-P_{\mathrm{sc}}(k+1)\right| \tag{30}$$

Fig. 7 illustrates the proposed MPC-based SESS control scheme. When U_{dc} exceeds the threshold $U_{\mathrm{dc}}^{\mathrm{thres}}$, the MPC-based SESS control is activated. The RSC current $I_{\mathrm{r}}(k)$, GSC current $I_{\mathrm{g}}(k)$, the actual DC-link voltage U_{dc} and voltage reference $U_{\mathrm{dc}}^{\mathrm{ref}}$ are first used to calculate the required SESS power. Meanwhile, the SC voltage and current, together with the actual DC-link voltage, will be used to predict the SC current $I_{\mathrm{sc}}(k+1)$, leading to two possible values of the SC power output according to (23). Then, the switching that minimizes (30) will be selected to control the bidirectional DC-DC converter. In this way, the DC-link voltages can be maintained stable during HVRT.

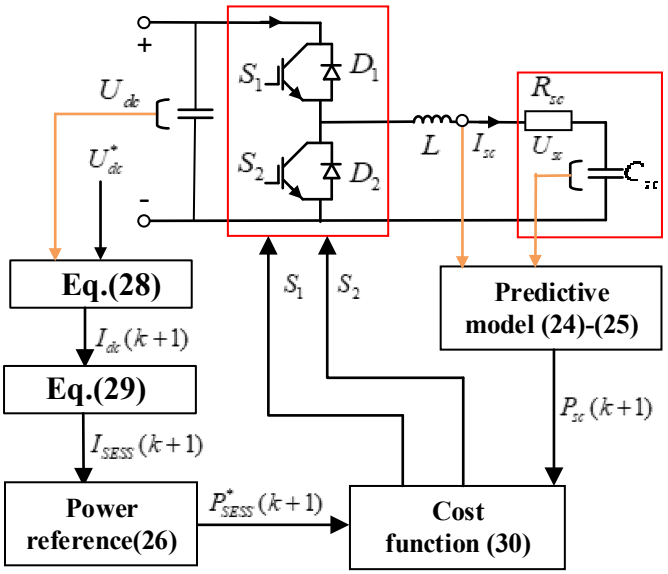

Fig. 7. Block diagram of MPC-based SESS control scheme.

4.2 Two-Stage Coordinated Control Scheme

Fig. 8 illustrates the two-stage CDVC strategy based on the above analyses. The proposed control scheme aims to achieve fast response for offshore wind turbines during HVRT. As can be seen in (16)-(17), the inductive reactive current injected must comply with grid code requirements. In the first stage, considering the dynamic behavior of the DFIG during HVRT, the VRCC scheme aims to supply fast reactive current support by regulating the current reference of the wind turbine. As can be seen in (21)-(22), the inductive reactive current injected from the GSC is limited with the range of the maximum allowable value. In the second stage, once the DC-link voltage exceeds the predefined threshold, the coordinated control scheme combining the SESS and the wind turbine operation is developed by using model predictive control (MPC), aiming to regulate the excessive active power by accurately tracking the current reference from the first stage.

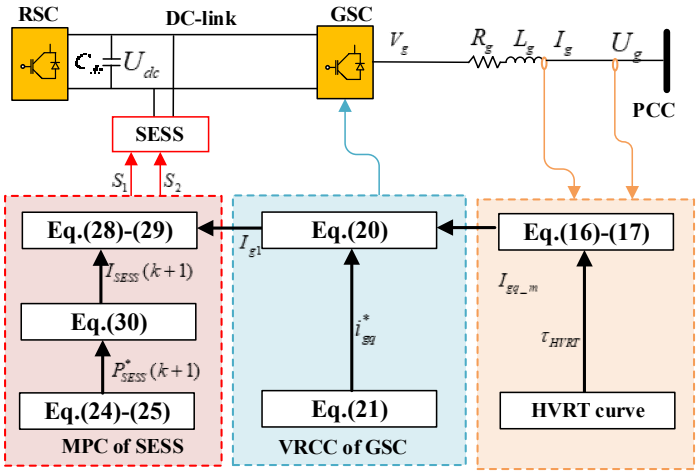

Fig. 8. Block diagram of the proposed CDVC control strategy.

Fig. 9 illustrates the implementation process of the proposed two-stage coordinated control strategy. In this study, to guarantee a fast imbalance power reduction and prevent DC-link overvoltage, the two-stage control scheme is designed based on the voltage swell severity and the depths of DC-link overvoltage. In particular, the DC-link voltage inhibition in the first stage is achieved by the VRCC strategy via compensating the reactive current, and the predictive model of active power output for the SESS is developed to handle DC-link overvoltage problem that has exceeded the threshold voltage in the second stage. The detailed process is summarized as follows: when a grid voltage swell event occurs and U_{g} exceeds the threshold value $U_{\mathrm{g}}^{\mathrm{thres}}$, the control system will determine whether the DC-link voltage is exceeding the normal value $U_{\mathrm{dc}}^{\mathrm{norm}}$. When U_{dc} exceeds the normal value $U_{\mathrm{dc}}^{\mathrm{norm}}$, the VRCC is activated by the GSC to provide fast reactive current support. If U_{dc} continues to rise and exceed the threshold value $U_{\mathrm{dc}}^{\mathrm{thres}}$, the MPC scheme is triggered to regulate the active power of the SESS for further mitigating the overvoltage of the DC-link. When U_{dc} decreases to the lower limit of the DC-link voltage $U_{\mathrm{dc}}^{\mathrm{lim}}$, the two-stage coordinated control is deactivated. Note that $U_{\mathrm{g}}^{\mathrm{thres}}$ is set to $1.1\ p.u.$, $U_{\mathrm{dc}}^{\mathrm{thres}}$ is set to $1.05\ p.u.$, and $U_{\mathrm{dc}}^{\mathrm{lim}}$ is set to $1.01\ p.u.$.

5. Case Study

In order to evaluate the effectiveness of the proposed control strategy, a model is established in PSCAD/EMTDC, which consists of a DFIG wind turbine, three power converters and their controllers, a DC-link capacitor, a SESS, and an equivalent power grid. The parameters of the DFIG and its control are given in Tables 1 and 2, respectively. In this simulation, the comparative analysis and discussion between the conventional chopper protection scheme [23], the proportional-integral (PI)-based SESS control scheme and the proposed scheme are tested using three simulation cases:

1) Case 1 is a symmetrical grid voltage swell of 1.3 $p.u.$ for 0.2 s;

2) Case 2 is a symmetrical grid voltage swell of 1.2 $p.u.$ for 0.2 s;

3) Case 3 is an asymmetrical grid voltage swell of 1.2 $p.u.$ for 0.2 s.

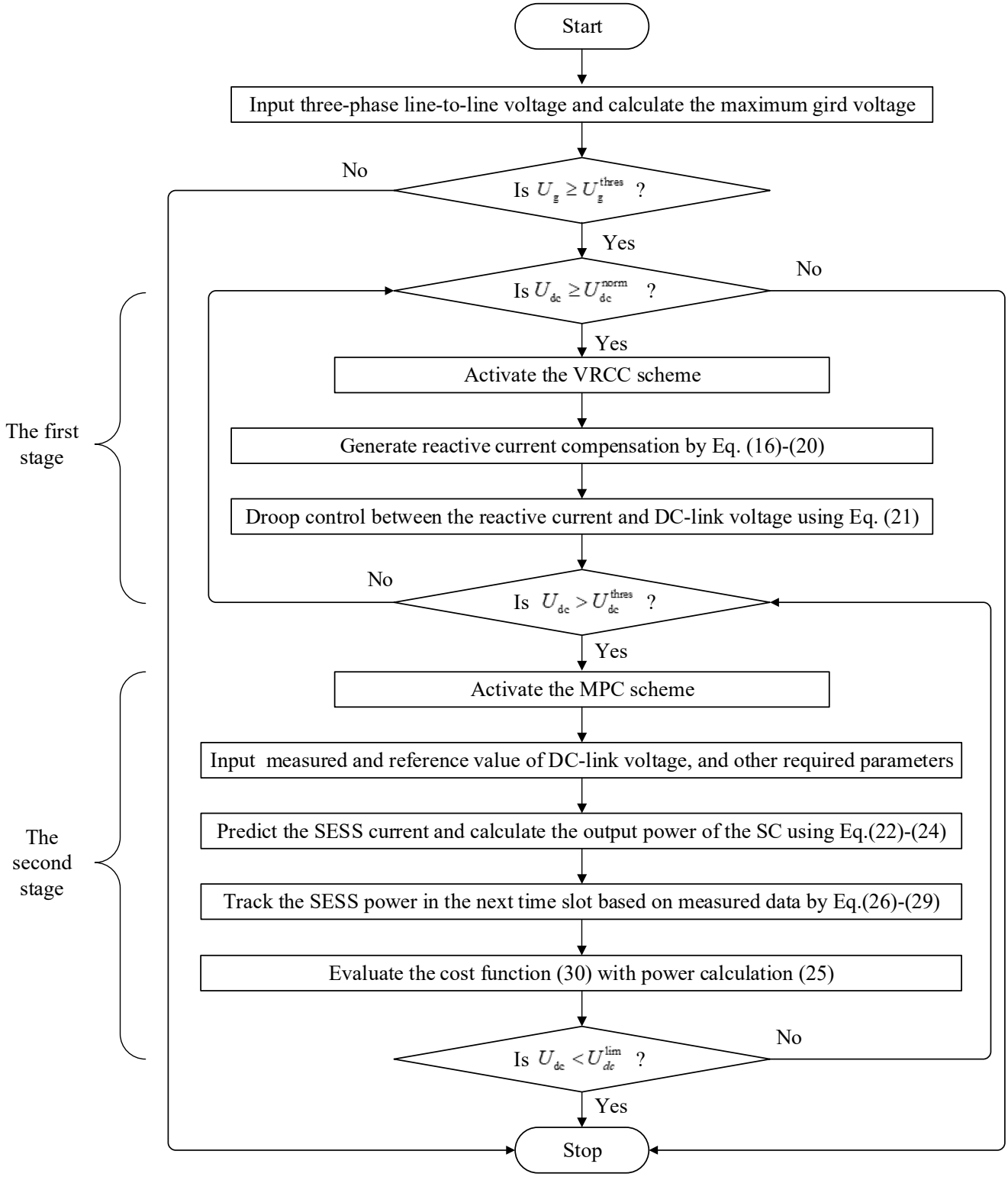

Fig. 9. Flowchart of the proposed two-stage CDVC control strategy.

Table 1 Parameters of Simulation

Parameters	Symbol	Value	Unit	Parameters	Symbol	Value	Unit
Rated power	P_{N}	2	MW	Rated frequency	f_{s}	60	Hz
Rated PCC voltage	V_{PCCN}	33	kV	Stator leakage inductance	L_{s}	0.100	$p.u.$
Rated stator voltage	V_{sN}	900	V	Rotor leakage inductance	L_{r}	0.110	$p.u.$
Rated rotor voltage	V_{rN}	690	V	Magnetizing inductance	L_{m}	4.5	$p.u.$
Rated DC-link voltage	U_{dc}	1450	V	GSC inductance	L_{g}	0.192	mH
Rated current of GSC	I_{gN}	1267.7	A	Stator resistance	R_{s}	0.0054	$p.u.$
Maximum output current of GSC	I_{gmax}	1521	A	Rotor resistance	R_{r}	0.00607	$p.u.$
Rated rotating speed	ω_{g}	376.99	rad/s	Inertia constant	H	6	s
DC-link capacitor	C_{dc}	7500	μF	Predefined threshold 1	$U_{\mathrm{dc}}^{\mathrm{thres}}$	1.05	$p.u.$
SESS capacitance	C_{sc}	19.25	F	Transmission cable length		30	km

Table 2 Control Parameters of GSC

Parameters	Symbol	Value	Parameters	Symbol	Value
DC voltage outer loop proportional gain	$\mathrm{k}'_{\mathrm{p1}}$	1	Reactive power outer loop proportional gain	$\mathrm{k}'_{\mathrm{p2}}$	2
DC voltage outer loop integral time constant	$\mathrm{k}'_{\mathrm{i1}}$	0.05	Reactive power outer loop integral time constant	$\mathrm{k}'_{\mathrm{i2}}$	0.02
D-axis current inner loop proportional gain	k_{p1}	2	Q-axis current inner loop proportional gain	k_{p2}	2
D-axis current inner loop integral time constant	k_{i1}	0.01	Q-axis current inner loop integral time constant	k_{i2}	0.025

5.1 *HVRT Performance of the Proposed Scheme*

In case 1, the voltage swell is assumed to start at t=2 s and last for 0.2 s. The performance of the proposed two-stage coordinated DC-link control scheme is simulated in Figs. 10-15. As can be seen from Fig. 10, the active power output of the DFIG wind turbine will increase when the grid voltage swell occurs and decrease when the event is cleared. The maximum active power deviation is approximately 35% P_{N}, which is much lower than 50% P_{N} required by the grid code. Fig.11 shows that the reactive power of the wind turbine decreases to a negative value at t=2 s. When the event is cleared at t=2.2 s, the reactive power increases to a positive value. The reason that the reactive power becomes negative is the inductive reactive current injection by the SESS.

Figs. 12 and 13 show that no major overshoots of the three-phase voltage and current at the PPC are observed since the SESS active power output is tightly controlled with the proposed MPC-based control strategy. Fig. 14 shows the terminal voltage swell of the wind turbine when the grid voltage swell is 1.3 $p.u.$. Fig. 15 shows that the response time of dynamic reactive current is less than 40 ms after the voltage swell occurs, which satisfies the requirement of reactive current support in Fig.3 (b).

Table 3 lists the comparative results of cases 1-3 on the peak value of active power, reactive power, PCC voltage, and PCC current. We can see that all parameters amplitude range and overshooting level in case 1 are the largest compared with cases 2 and 3. Taking the PCC current I_{gm} for example, the peak voltage in case 1 is about 0.18 kA, which is increased by 50% than case 2, and 100% than case 3. The reason for a larger peak value during the HVRT is that case 1 is the most serious voltage swell condition that occurs in offshore wind farms, which satisfies the magnitude requirement of the grid code.

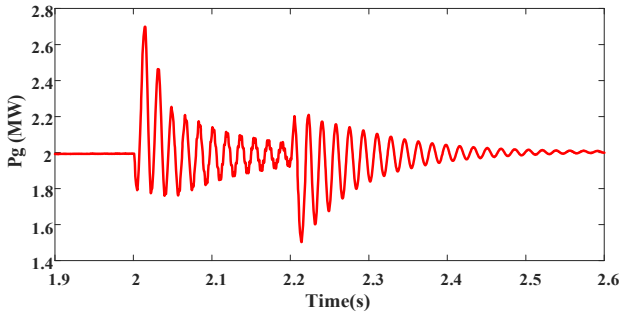

Fig. 10. Active power of the wind turbine terminal in case 1

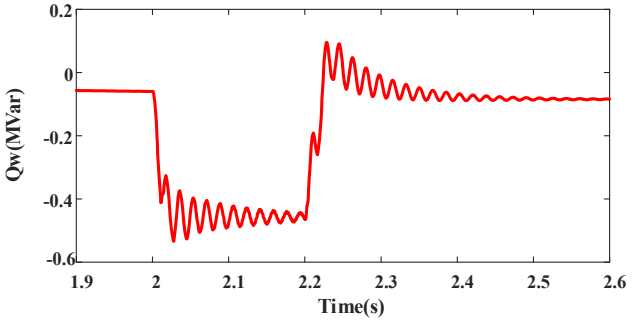

Fig. 11. Reactive power of the wind turbine terminal in case 1.

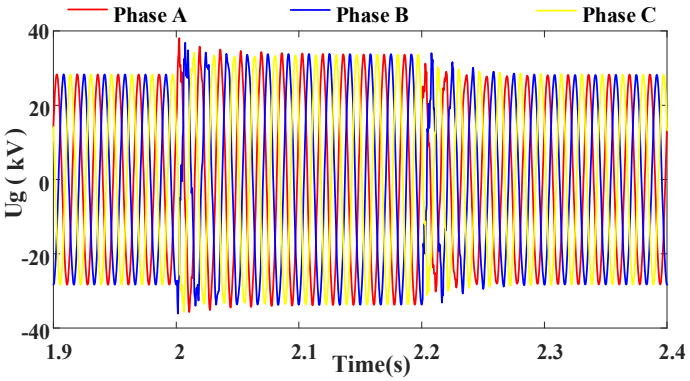

Fig. 12. PCC voltage curve in case 1.

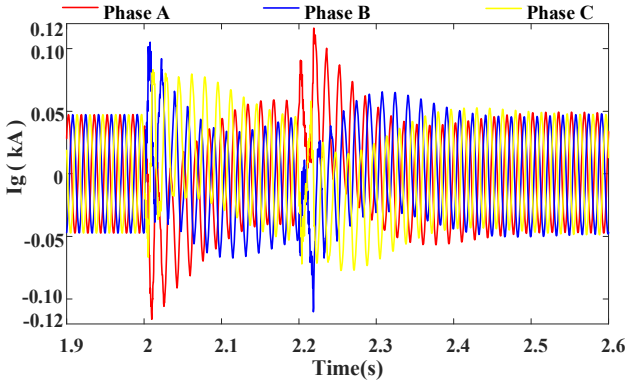

Fig. 13. PCC current curve in case 1.

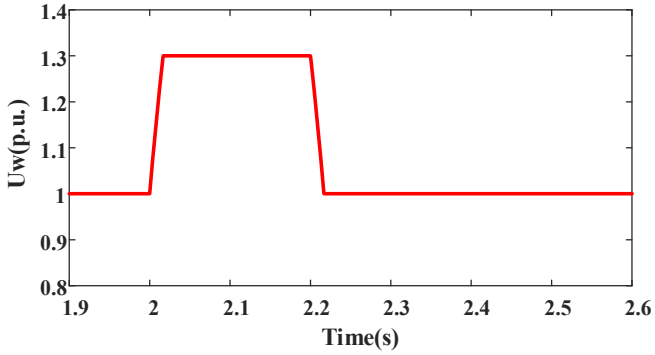

Fig. 14. Terminal voltage of wind turbine in case 1.

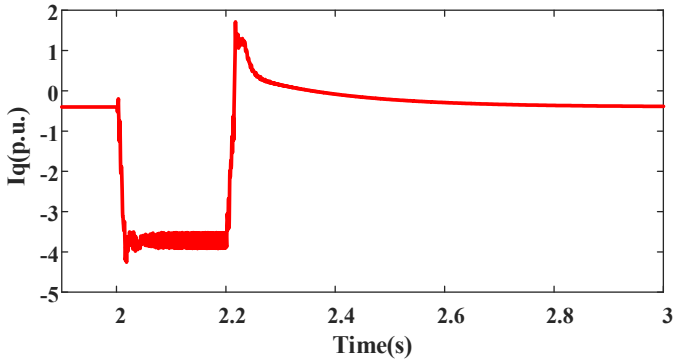

Fig. 15. Reactive current injection of wind turbine in case 1.

Table 3 Comparative Analysis of Other Parameters of Cases 1-3

Cases	P_g(MW)	Q_g(MVA)	U_{gm}(kV)	I_{gm}(kA)
Case 1	2.7	-0.55	40	0.18
Case 2	2.53	-0.39	38	0.12
Case 3	2.26	-0.24	32	0.09

5.2 Comparative Results and Analysis

For in-depth investigations on the effectiveness and superiority of the proposed methodology, three schemes are considered for comparative analysis and discussions. The comparative result and analysis between three schemes are shown in Figs. 16-18.

1) Scheme 1 is the traditional single-stage chopper control scheme;

2) Scheme 2 is the PI controlled SESS control scheme;

3) Scheme 3 is the proposed two-stage CDVC control scheme.

The comparative results of the D-axis current of the GSC as well as DC-link voltage with schemes 1 and 3 in case 1 are shown in Fig. 16. When a grid voltage swell occurs, the D-axis current of the GSC is controlled to regulate the DC-link voltage. As shown in Fig. 16(a), D-axis current overshoots of the GSC with scheme 1 are much larger than those with scheme 3. In Fig. 16(b), the DC-link voltage with scheme 1 has the larger overshoots compared with scheme 3. The effect of grid voltage swell on DC-link voltage amplitude is slightly mitigated with the proposed control scheme.

Fig. 17 depicts the comparative performances between schemes 1 and 3 in case 2. As can be seen in Fig. 17(a), the D-axis current of the GSC overshoot with the SESS scheme is lower than that with the chopper scheme, since the SC output power in the next time slot is real-time tracked to the predictive SESS output power with MPC strategy. In Fig. 17(b), without the connection of the SESS unit, the voltage across DC-link capacitor will experience significant oscillations and overshooting levels during voltage swell incidence in the chopper scheme.

Fig. 18 illustrates the comparative performances with schemes 1 and 3 in case 3. It can be found in Fig. 18(a), the fluctuating scope of the D-axis current of the GSC with the proposed scheme is the smallest during the HVRT period, which is only 10% peak voltage of the case 2. Fig. 18(b) shows that, compared to the chopper scheme, the DC-link peak voltage is reduced by 50% and its oscillations level is significantly reduced under the CDVC control strategy. The proposed control scheme can tackle the inrush-current impact from gird voltage swell on offshore wind turbines, and thereby facilitate the DC-link voltage to maintain stability with smaller overshoots.

To verify the performance of the proposed two-stage CDVC control strategy, the comparison of schemes 1-3 is shown in Fig. 19. As shown in Figs. 19(a)-19(b), the stator current has a fast transient recovery after the event occurrence whereas the rotor current oscillation amplitude is large during the HVRT period. In Fig. 19(c), the D-axis current of the GSC with the CDVC control strategy is evidently smaller than that with other schemes. For better observation, the zoom-in waveform of the U_{dc} at 2 s is re-plotted in Fig. 19(d). Compared to the conventional chopper control and PI-controlled SESS control scheme, the proposed method has a better and faster transient performance, and the effect of grid voltage swell on DC-link voltage amplitude is slightly mitigated.

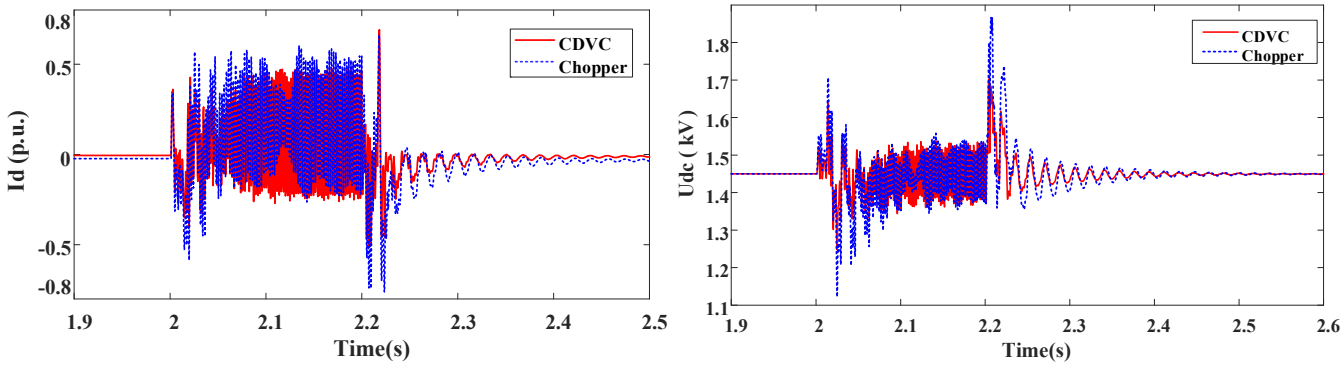

(a) D-axis current of the GSC (b) DC-link voltage.

Fig. 16. The comparative results with schemes 1 and 3 in case 1.

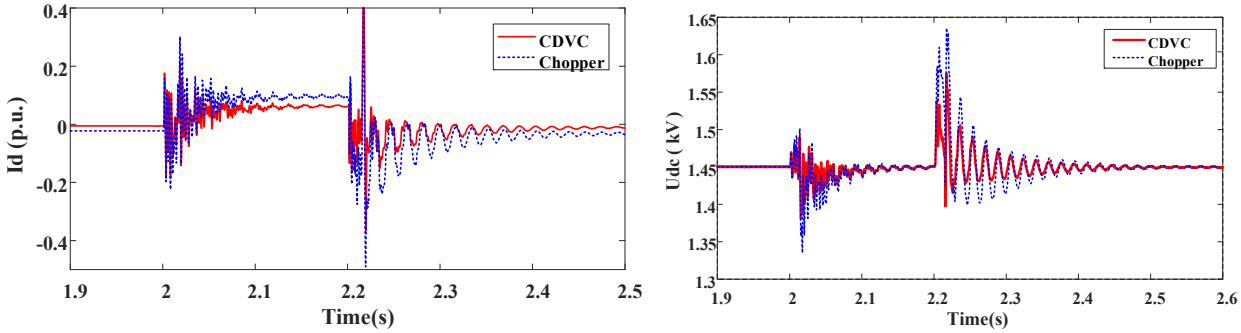

(a) D-axis current of the GSC (b) DC-link voltage

Fig. 17. The comparative results with schemes 1 and 3 in case 2.

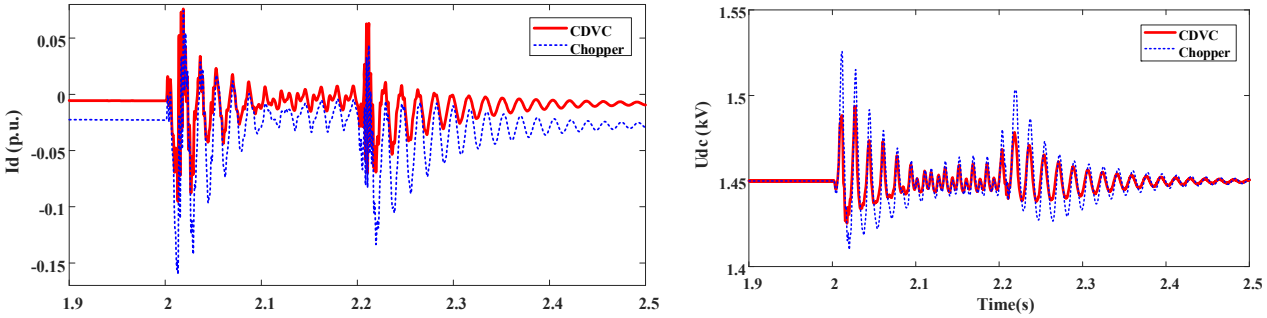

(a) D-axis current of the GSC (b) DC-link voltage

Fig. 18. The comparative results with schemes 1 and 3 in case 3.

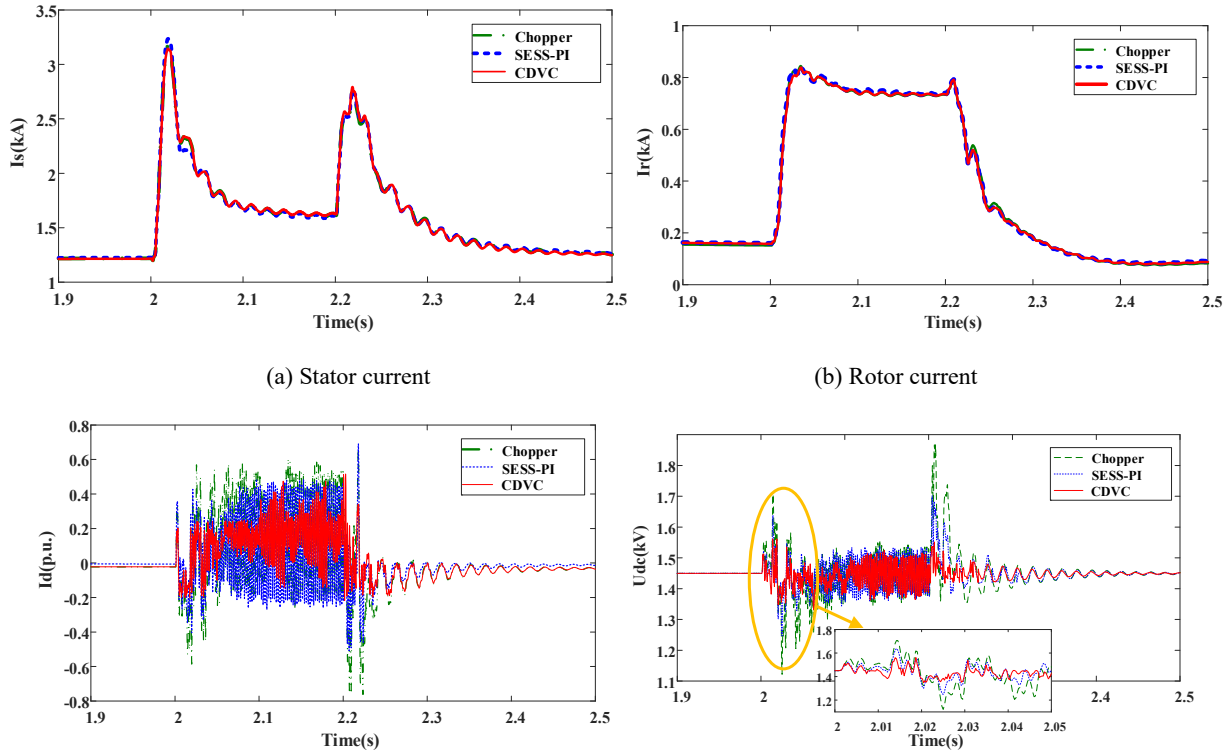

(a) Stator current (b) Rotor current

(c) D-axis current of the GSC (d) DC-link voltage

Fig. 19. Case study results with schemes 1-3 in case 1.

6. Conclusion

In this paper, a two-stage CDVD strategy is proposed to inhibit the effect of DC-link overvoltage on converters when the grid voltage swells. To tightly control the DC-link voltage, a VRCC scheme is proposed for offshore wind turbines to achieve a fast reactive current compensation by coordinating with the MPC scheme of the SESS. The significant improvements of the proposed scheme are due to the controllable characteristic of reactive current and active power in various magnitudes and timescales of voltage swell for flexible regulation of DC-link voltage. The simulations show that the proposed control scheme effectively relieves the DC-link voltage oscillation during HVRT and the overshoot of injected reactive current with the SESS scheme is much lower than that with other conventional control schemes. Especially for asymmetrical voltage swells, the peak value of DC-link voltage is reduced by 50%, and overshoots are also significantly reduced compared with the chopper scheme and traditional PI control.

Acknowledgements

The authors gratefully acknowledge the support of the National Natural Science Foundation of China (51722701, 51877072), and the China Scholarship Council (201906130083).

References

[1] Global Wind Energy Council, Brussels, Belgium, Global Wind Statistics, 2018.

[2] Diaz M, Cardenas R, Espinoza M, and Mora F. Control of wind energy conversion systems based on the modular multilevel matrix converter. IEEE Trans Ind Electron 2017; 64(11): 8799-8810.

[3] Wang P, Zhang Z, Sahni M, and Huang Q. Improved wind farm aggregated modeling method for large-scale power system stability studies. IEEE Trans Power Syst 2018; 33(6): 6332-6342.

[4] Guo Y, Gao H, and Wu Q. Distributed cooperative voltage control of wind farms based on consensus protocol. Int J Electr Power Energy Syst 2019;104:593–602.

[5] Huang S, Li P, Wu Q, Li F, and Rong F. ADMM-based distributed optimal reactive power control for loss minimization of DFIG-based wind farms. Int. J. Electr. Power Energy Syst 2020; 118: 105827.

[6] Xu D, Wu Q, Zhou B, and Li C. Distributed multi-energy operation of coupled electricity, heating and natural gas networks. IEEE Trans Sustain Energy 2020; DOI: 10.1109/TSTE.2019.2961432, in press.

[7] Baqi O and Nasiri A. Series voltage compensation for DFIG wind turbine low-voltage ride-through solution. IEEE Trans Energy Convers 2011; 26(1): 272-280.

[8] Guo Y, Gao H, Wu Q, Østergaard J, Yu D, Shahidehpour M. Distributed coordinated active and reactive power control of wind farms based on model predictive control. Int J Electr Power Energy Syst 2019;104:78–88.

[9] Xie D, Xu Z, and Yang L. A comprehensive LVRT control strategy for DFIG wind turbines with enhanced reactive power support. IEEE Trans Power Syst 2013; 28(3): 3302-3310.

[10] Jiao W, Wu Q, Huang S, and Chen J. Decentralized voltage control of wind farm based on gradient projection method. Int J Electr Power Energy Syst 2020;123:106308.

[11] Alia M, Mehmoodb K, Balocha S, and Kima C. Modified rotor-side converter control design for improving the LVRT capability of a DFIG-based WECS. Int. J. Electr. Power Energy Syst 2020; 186: 106403.

[12] Han J, Kong X, Li P, and Zhang Z. A novel low voltage ride through strategy for cascaded power electronic transformer. Protect Control Mod Power Syst 2019; 4 (20): 1-12.

[13] Li W, Zhu M, Chao P, Liang X, and Xu D. Enhanced FRT and post-fault recovery control for MMC-HVDC connected offshore wind farms. IEEE Trans Power Syst 2020; 35(2): 1606–1617.

[14] Raza M, Collados C, and Gomis-Bellmunt O. Reactive power management in an offshore AC network having multiple

voltage source converters. Appl Energy 2017; 206:793-803.
[15] Ruan J, Lu Z, Qiao Y, and Min Y. Analysis on applicability problems of the aggregation-based representation of wind farms considering DFIGs' LVRT behaviors. IEEE Trans Power Syst 2016; 31(6): 4953 – 4965.
[16] Zhou Q, Cheng Y, and Bian X. Analysis of restrike overvoltage of circuit breakers in offshore wind farms. IEEE Trans Appl Supercond 2016; 26(7):1–5.
[17] Huang S, Wu Q, Guo Y, and Lin Z. Bi-level decentralized active and reactive power control for large-scale wind farm cluster. Int. J. Electr. Power Energy Syst 2019; 111: 201-215.
[18] Vittal E, O'Malley M, and Keane A. A steady-state voltage stability analysis of power systems with high penetrations of wind. IEEE Trans Power Syst 2010; 25(1): 433-442.
[19] Mansour M, Mohammad M, and Islam S. Low and high voltage ride-through of DFIG wind turbines using hybrid current controlled converters. Electr Power Syst Res 2011; 81(7): 1456-1465.
[20] Feltes C, Engelhardt S, Kretschmann J. High voltage ride through of DFIG based wind turbines. Proc IEEE Power Energy Soc Gen Meet. 2008: 1-8.
[21] Xie Z, Zhang X, and Zhang X. Improved ride-through control of DFIG during grid voltage swell. IEEE Trans Ind Electron 2015; 62(6): 3584-3594.
[22] Li S, Xu L, and Haskew T. Control of VSC-based STATCOM using conventional and direct-current vector control strategies. Int J Electr Power Energy Syst 2013;45(1):175–86.
[23] Guo Y, Gao H, Wu Q, Zhao H, and Ostergaard J. Enhanced voltage control of VSC-HVDC connected offshore wind farms based on model predictive control. IEEE Trans Sustain Energy 2018; 9(1): 474-487.
[24] Yang J, Fletcher J, and Reilly J. A series dynamic resistor based converter protection scheme for doubly fed induction generator during various fault conditions. IEEE Trans Energy Covers 2010; 25(2): 422-432.
[25] Jiang Q and Hong H. Wavelet-based capacity configuration and coordinated control of hybrid energy storage system for smoothing out wind power fluctuations. IEEE Trans Power Syst 2013; 28 (2): 1363-1372.
[26] Yunus A, Masoum M, and Siada A. Application of SMES to enhance the dynamic performance of DFIG during voltage sag and swell. IEEE Trans Appl Supercond 2012; 22(4): 1-6.
[27] Mendis N, Muttaqi K, and Perera S. Management of battery-supercapacitor hybrid energy storage and synchronous condenser for isolated operation of PMSG based variable-speed wind turbine generating systems. IEEE Trans Smart Grid 2014; 5(2): 944-953.
[28] Huang S, Wu Q, Guo Y, and Rong F. Optimal active power control based on MPC for DFIG-based wind farm equipped with distributed energy storage systems. Int. J. Electr. Power Energy Syst 2019; 113: 154–163.
[29] Barton J and Infield D. Energy storage and its use with intermittent renewable energy. IEEE Trans Energy Convers 2004; 19(2): 441-448.
[30] Wee K, Choi S, and Vilathgamuwa D. Design of a least-cost battery-supercapacitor energy storage system for realizing dispatchable wind power. IEEE Trans Sustain Energy 2013; 4(2): 786-796.
[31] Australian Energy Market Commission, National electricity rules version 122[R/OL][2019-05-30].[Online]. Available: http://www. aemc. gov. au.
[32] E.O.N. Netz. Grid code-high and extra high voltage. E. ON Netz GmbH, Bayreuth, Apr.2006.
[33] Jin R, Hou P, Yang G. Cable routing optimization for offshore wind power plants via wind scenarios considering power loss cost model. Appl Energy 2019; 254: 113719.
[34] Liu X, Li C, and Shahidehpour M. Fault current hierarchical limitation strategy for fault ride-through scheme of microgrid. IEEE Trans Smart Grid 2019; 10(6): 6566-6579.